Thin-Walled Structures 182 (2023) 110242

Contents lists available at ScienceDirect

Thin-Walled Structures

journal homepage: www.elsevier.com/locate/tws

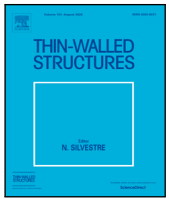

Full length article

Aluminium alloy channel columns: Testing, numerical modelling and design

Evangelia Georgantzia *, Michaela Gkantou, George S. Kamaris

School of Civil Engineering and Built Environment, Liverpool John Moores University, United Kingdom

ARTICLE INFO

Keywords:
Aluminium alloys
Channel sections
Stub column tests
Flexural buckling
Numerical modelling
Eurocode 9
Direct Strength Method

ABSTRACT

Aluminium alloys can be employed in a wide range of structural applications offering high strength-to-weight ratio, whilst they can easily be extruded in various shapes. Channel (C-) sections have been increasingly employed as compression members, such as wall studs and chord members of roof trusses in framed residential and commercial buildings. However, relevant studies on their compressive behaviour are quite limited and thus a greater emphasis should be placed on providing a deeper understanding. Towards this direction, this paper examines the structural performance of C-sections under axial compression. An experimental and numerical investigation was performed on 6082-T6 heat-treated aluminium alloy C-section columns. In total, 6 fix-ended stub column tests were executed to examine the cross-sectional compressive behaviour, whilst 8 pin-ended column tests were conducted to study their minor-axis flexural buckling behaviour. The obtained experimental results were utilised to validate the developed finite element models. Subsequently, extensive parametric studies were carried out to generate additional performance data over a broad range of cross-sectional aspect ratios, and cross-sectional and member slendernesses. Both the experimentally and numerically obtained ultimate strengths are utilised to assess the accuracy of Eurocode 9 design provisions, including the flexural buckling curve. On the basis of the experimental and numerical results, a new flexural buckling curve is proposed improving the design accuracy. The applicability of the Direct Strength Method on the design of aluminium alloy C-sections subjected to axial compression is also evaluated resulting in the most accurate and consistent design strength predictions.

1. Introduction

Aluminium is the third – behind oxygen and silicon – on the list of the most abundant elements comprising roughly the 8% of the earth's crust [1]. Aluminium is a versatile metal that could offer advantages over other structural materials by proper alloying and treatment. Particularly, 6000 series aluminium alloys, known as structural alloys, have high strength-to-weight ratio being able to meet the strength requirements, whilst reducing the structure's self-weight. Therefore, they could be a suitable material choice for high-rise buildings, e.g., skyscrapers and long-span structures, e.g., roof systems and bridges. Moreover, 6000 series aluminium alloys are corrosion-resistant and immune to harmful effects of ultraviolet radiation, ensuring optimal performance over a long lifetime. They are also well suited to the extrusion process due to high plasticity at the extrusion temperature and thus they could be supplied in various complex shapes. Amongst the different available cross-sectional shapes, channel (C-) sections have been increasingly employed as compression members, such as wall studs and chord members of roof trusses in framed residential and commercial buildings. A C-section column as a thin-walled member, when is subjected to compressive loading may exhibit instability phenomena, which limit its load-carrying capacity. These instability phenomena include deformations at cross-sectional level, i.e., local or distortional buckling, deformations at member level, i.e., flexural or flexural–torsional buckling, or a combination of these buckling modes. Consequently, instability phenomena should be considered when designing a thin-walled structural member against compressive loading.

To date, several experimental and numerical studies have been reported on the buckling response of cold-formed steel plain and lipped C-sections under pin- and fix-ended support conditions [2–8]. Moreover, Yang and Hancock [9] performed a series of compression tests on lipped channel columns fabricated from G550 MPa high strength steel. The obtained results demonstrated the significant influence of the local and distortional interactive buckling mode on the ultimate strength of the columns. Evaluation of the effective width method [10] and the Direct Strength Method (DSM) [11] also denoted overestimation of the actual load-carrying capacity which owes to the fact that both design approaches do not account for the interaction between local and distortional buckling within the calculations. Becque and Rasmussen [12] carried out an extensive parametric study on the local and global interactive buckling behaviour of stainless steel lipped channel columns. The obtained results were utilised to assess the international

* Corresponding author.
E-mail address: E.Georgantzia@2019.ljmu.ac.uk (E. Georgantzia).

https://doi.org/10.1016/j.tws.2022.110242
Received 9 June 2022; Received in revised form 10 August 2022; Accepted 8 October 2022
Available online xxxx

design rules which were found to be quite conservative. In a more recent study, Wang et al. [13] examined the cross-sectional behaviour of press-braked S960 ultra-high strength steel C-section columns and assessed the applicability of the existing codified design provisions. On the basis of the experimental results, revised design formulae were proposed enabling for safe, accurate and consistent design strength predictions. Following, Wang et al. [14] extended the investigation on S960 ultra-high strength steel C-sections by testing pin-ended columns prone to flexural buckling about the minor axis. Additionally, Zhang et al. [15] reported a series of stub column tests on press-braked S690 high strength steel C-sections. Based on the experimental results and those obtained from a supplementary numerical study, it was found that Eurocode's [16] Class 3 slenderness limit for welded and hot-rolled high strength steel outstand plate elements could be adopted for their press-braked counterparts. Zhang et al. [17] conducted stub column tests on press-braked stainless steel C-sections to determine their local buckling behaviour and the cross-sectional capacities. In a following study [18], the same researchers examined the minor-axis flexural buckling response of press-braked stainless steel C-section columns employing pin-ended support conditions. The obtained flexural buckling strengths were compared with those derived from the international design codes revealing that in most cases the codified predictions are unsafe. Unlike steel C-sections, the reported research studies on the buckling response of aluminium alloy C-sections are rather limited [19]. Zhu et al. [20] tested 28 plain and lipped channel columns made from 6061-T6 and 6063-T5 aluminium alloys under fixed-end support conditions. The resulting test data were utilised to evaluate the current design specifications as well as the Continuous Strength Method (CSM) [21] and the DSM [22]. Relative comparisons showed that the latter two design methods provide more accurate and consistent design strength predictions. The reported results were utilised in a following study by Zhu et al. [23] to investigate numerically the buckling behaviour of welded C-section columns. Modified CSM and DSM approaches considering the heat-affected zone softening effects due to welding were also proposed.

The fixed-end and pin-ended support conditions are the two limiting support conditions for columns of non-sway frames affecting differently the overall behaviour of the columns [3]. According to the literature review, there are no reported studies on the buckling behaviour of aluminium alloy C-section columns under pin-ended support conditions. To address this research gap, a comprehensive experimental programme was carried out to investigate the structural performance of aluminium alloy C-sections under concentric compression. On this direction, 6 fix-ended stub column tests and 8 minor-axis pin-ended column tests were performed employing 7 different C-sections fabricated from 6082-T6 heat-treated aluminium alloy, as presented in Section 2. Prior to testing, the geometric dimensions and initial geometric imperfection amplitudes were measured and reported herein. Tensile coupon tests were also conducted to determine the mechanical properties of the examined aluminium alloy. In Section 3, the experimental results were utilised to verify the developed finite element (FE) models, which were subsequently employed in a wide parametric study to derive further structural performance data over a broad range of cross-sectional aspect ratios, and cross-sectional and member slendernesses. In Section 4, the experimentally and numerically obtained ultimate strengths were utilised to assess the accuracy of the Eurocode 9 (EC9) [24] and the applicability of the DSM [25] on the design of aluminium alloy C-sections subjected to concentric axial compression. The conclusions are summarised in Section 5.

2. Experimental programme

The experimental investigation was performed in the Light Structures and Materials Laboratory of the School of Civil Engineering and Built Environment at Liverpool John Moores University.

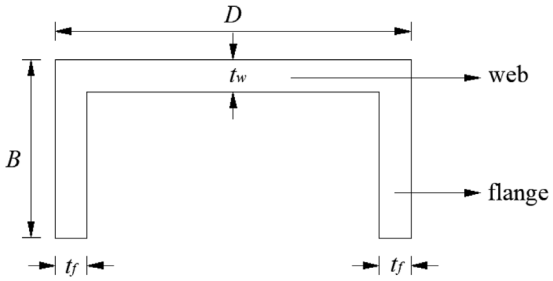

Fig. 1. Adopted notation for C-sections.

2.1. Test specimens and geometric imperfection measurements

A series of fix-ended stub column tests was carried out employing 6 different cross-sections to study the cross-sectional behaviour of channels. Particularly, the slenderness ratio β_f/ε of the slenderest plate element, i.e., outstand flange, was ranging from 5.46 to 11.94, where $\beta_f = (B - t_w/2)/t_f$ is the slenderness parameter and $\varepsilon = \sqrt{250/\sigma_{0.2}}$. B is the outer width of the flange, t_w is the web thickness, t_f is the flange thickness and $\sigma_{0.2}$ is the 0.2% proof stress. The specimens' nominal length was set equal to three times the maximum cross-sectional dimension enabling for pure local buckling behaviour without any coupled instability phenomena [26]. Fig. 1 depicts the adopted notation for the examined C-sections.

Upon establishing the cross-sectional response, 8 concentric compression tests were performed to examine the minor-axis buckling behaviour. The tests were carried out on pin-ended columns in 2 different nominal lengths L, namely 300 mm and 500 mm. These lengths allowed to cover a broad range of member slendernesses $\overline{\lambda}$ from 0.22–1.32, where $\overline{\lambda} = \sqrt{A\sigma_{0.2}/N_{cr}}$; A is the cross-sectional area and N_{cr} is the elastic critical buckling load of the column.

Prior to testing, the geometrical dimensions of the examined specimens were measured and are listed in Tables 1 and 2 for fix-ended stub and pin-ended columns, respectively, where D is the outer web depth. The specimens were labelled according to the nominal geometric dimensions of the sections followed by the specimen's nominal length, i.e., $D \times B \times t$-L (where $t = t_w = t_f$ is the nominal thickness of both web and flanges). Table 2 also reports the buckling length values (L_e) and the applied eccentricities values (e_0, e_m), which will be explained in Section 2.4.

The initial geometric imperfections inherently present in thin-walled structural members may significantly affect their structural behaviour and ultimate strength triggering buckling phenomena [20,27–30].

Therefore, the initial local ω_l and global ω_g geometric imperfections for each specimen were measured before the execution of the tests. Each specimen was mounted onto a flat granite surface table and the measurements were taken using a Mitutoyo linear height gauge. A ball probe attached onto the scribing jaw was moving along the centreline of each constituent plate element, i.e., internal web and both outstand flanges, over the full specimen's length. The measuring points were defined at 10 mm intervals. For each constituent plate element, the maximum deviation of the measuring points from a flat datum plane was recorded and the maximum recorded value was defined as the initial local geometric imperfection amplitude ω_l of the specimen [31]. Note that for the fix-ended stub columns only the ω_l amplitudes were recorded, as they are sufficiently short to preclude the influence of the ω_g on the structural behaviour, whilst they are sufficiently long to incorporate a representative pattern of the ω_l to be present in the examined specimen [26]. For the initial global geometric imperfections ω_g related to the examined buckling axis, i.e., minor axis, the measurements were recorded along two longitudinal lines of the internal web. The deviation of the measuring point at the mid-height from a linear

Table 1
Mean measured geometric dimensions of fix-ended stub columns.

Specimen	D (mm)	B (mm)	t_w (mm)	t_f (mm)	β_f/ε	L (mm)	ω_l (mm)
50.8 × 50.8 × 6.35-L150	50.92	50.84	6.28	6.32	7.49	152.76	0.28 (t_f/23)
50.8 × 50.8 × 4.76-L150	50.89	50.56	4.62	4.75	10.42	152.67	0.30 (t_f/16)
50.8 × 38.1 × 6.35-L150	50.89	38.23	6.32	6.35	5.46	152.66	0.35 (t_f/18)
50.8 × 38.1 × 3.18-L150	50.81	37.75	3.13	3.13	11.94	152.42	0.26 (t_f/12)
50.8 × 25.4 × 3.18-L150	50.68	25.85	3.17	3.11	7.62	152.03	0.27 (t_f/12)
38.1 × 38.1 × 4.76-L115	37.97	37.97	4.68	4.64	7.84	113.92	0.31 (t_f/15)

Table 2
Mean measured geometric dimensions of pin-ended columns.

Specimen	D (mm)	B (mm)	t_w (mm)	t_f (mm)	L (mm)	L_e (mm)	$\bar{\lambda}$	ω_l (mm)	ω_g (mm)	e_0 (mm)	$e_m = \omega_g + e_0$ (mm)
50.8 × 50.8 × 6.35-L500	50.92	50.84	6.35	6.32	500.50	564.50	0.63	0.27 (t_f/23)	−0.05 (−L_e/11290)	−0.21 (−L_e/2688)	−0.26 (−L_e/2171)
76.2 × 76.2 × 6.35-L500	76.28	76.26	6.17	6.29	500.00	564.00	0.36	0.33 (t_f/19)	0.11 (L_e/5127)	0.32 (L_e/1763)	0.43 (L_e/1312)
76.2 × 76.2 × 6.35-L300	76.28	76.26	6.19	6.29	300.80	364.80	0.22	0.22 (t_f/29)	0.09 (L_e/4053)	0.26 (L_e/1403)	0.35 (L_e/1042)
50.8 × 38.1 × 6.35-L500	50.89	38.13	6.30	6.35	500.00	564.00	0.90	0.20 (t_f/32)	0.13 (L_e/4338)	0.32 (L_e/1763)	0.45 (L_e/1253)
50.8 × 38.1 × 3.18-L500	50.81	37.95	3.08	3.13	500.50	564.50	0.79	0.24 (t_f/13)	0.08 (L_e/7056)	0.17 (L_e/3321)	0.25 (L_e/2258)
50.8 × 38.1 × 3.18-L300	50.81	37.95	3.08	3.13	300.00	364.00	0.48	0.18 (t_f/17)	0.04 (L_e/9100)	0.28 (L_e/1300)	0.32 (L_e/1138)
50.8 × 25.4 × 3.18-L500	50.68	25.43	3.14	3.11	500.00	564.00	1.32	0.22 (t_f/14)	0.07 (L_e/8057)	0.20 (L_e/2820)	0.27 (L_e/2089)
50.8 × 25.4 × 3.18-L300	50.68	25.43	3.15	3.11	300.30	364.30	0.79	0.26 (t_f/12)	0.06 (L_e/6072)	0.19 (L_e/1917)	0.25 (L_e/1457)

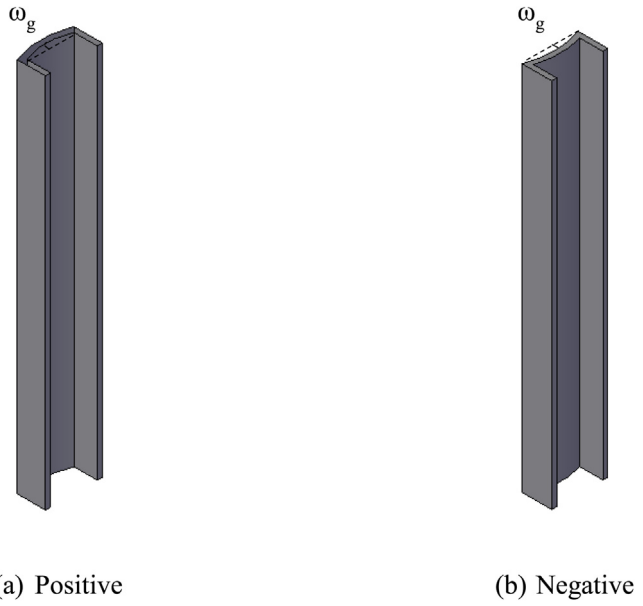

Fig. 2. Sign convention for measured initial global geometric imperfection amplitude ω_g.

reference line connecting the corresponding measuring points at both ends was recorded and the maximum of the two recorded values was defined as the initial global geometric imperfection amplitude ω_g of the specimen [32]. Note that the measured ω_g was considered as positive if the column specimen initially bows towards the web and negative if the column specimen initially bows towards the flange tips, as displayed in Fig. 2. The measured ω_l and ω_g amplitudes are included in Tables 1 and 2 for fix-ended stub and pin-ended columns, respectively, and will be employed in the numerical study described in Section 3.

2.2. Aluminium 6082-T6: tensile coupon tests

The material properties of the examined 6082-T6 heat-treated aluminium alloy were determined through tensile coupon tests. For each examined C-section, two flat coupons were extracted and were machined in line with the geometric requirements specified in EN ISO 6892-1 [33]. A 50 kN Tinius Olsen testing machine was used for the execution of the tests, applying a displacement rate of 0.2 mm/min. An extensometer, shown in Fig. 3(a), was also attached to the central necked part of the coupon to measure the longitudinal strains during testing. All tested coupons after testing are depicted in Fig. 3(b).

The experimentally obtained engineering stress–strain ($\sigma-\varepsilon$) curves for each examined C-section are plotted in Fig. 4. As can be seen, the tested coupons exhibited a rounded nonlinear stress–strain behaviour with continuous strain hardening. In the absence of a distinct yield point, a 0.2% offset is employed to obtain an approximate yield point. Table 3 summarises the measured material properties, including the initial modulus of Elasticity E, the 0.1% proof stress $\sigma_{0.1}$, the 0.2% proof stress $\sigma_{0.2}$, the ultimate tensile stress σ_u, the strain corresponding to ultimate tensile stress ε_u, the strain at fracture ε_f, the strain hardening exponent n given in Ramberg–Osgood material model [34,35] and the strain hardening ratio $\sigma_u/\sigma_{0.2}$. According to EC9 [24], the expected values for E, $\sigma_{0.2}$, σ_u, ε_u, ε_f, n and $\sigma_u/\sigma_{0.2}$ are 70 000 MPa, 250 MPa, 290 MPa, 8%, 13%, 32 and 1.16, respectively. Note that the experimentally derived material properties for each studied cross-section will be employed in the numerical study described in Section 3.2.

2.3. Fix-ended stub column tests

A total of 6 fix-ended stub column tests were performed to investigate the cross-sectional response of aluminium alloy C-sections. Fig. 5 shows a schematic illustration of the test arrangement and the corresponding employed instrumentation. The specimens were cut roughly to length and then were milled flat at both ends to a tolerance of ±0.02 mm to achieve uniform distribution of the applied compressive loading. A Mayes servo-controlled hydraulic testing machine with 600 kN maximum capacity was used for the execution of the tests. The end plates of the testing machine were fixed flat and parallel. Alignment of the examined specimens was deemed necessary to ensure that the compressive loading is applied concentrically. To do so, special wooden cut-outs were placed at both ends to accurately locate the specimens. Following, an initial compressive loading approximately equal to 15% of the predicted load-carrying capacity was applied [36] and the variation in strains taken from the affixed strain gauges at the mid-length of the specimen was observed. In all tested specimens, the variation between strains from the average strain was less than 5% [37] confirming that the compressive loading was applied concentrically. Moreover, linearity of the stress–strain curve was utilised to verify that the initial compressive loading was below the proportional limit. Underpinning bolts were inserted between the flanges and G-clamps were located onto the outer faces of the flanges at both ends to prevent any localised failure [15]. The compressive loading was applied at a cross-head displacement rate of 0.2 mm/min.

The experimental setup for a typical fix-ended stub column test is depicted in Fig. 6. Two linear variable displacement transducers

Fig. 3. Tensile coupon specimens.

Table 3
Material properties obtained from tensile coupon tests.

Specimen	E (MPa)	$\sigma_{0.1}$ (MPa)	$\sigma_{0.2}$ (MPa)	σ_u (MPa)	ε_u (%)	ε_f (%)	n	$\sigma_u/\sigma_{0.2}$
50.8 × 50.8 × 6.35	66 729	275	282	324	7.5	13.5	27.6	1.15
50.8 × 50.8 × 4.76	69 302	284	292	332	9.1	12.9	25.0	1.14
76.2 × 76.2 × 6.35	70 885	280	286	317	8.8	16.2	32.7	1.11
50.8 × 38.1 × 6.35	67 009	290	298	334	7.5	12.7	25.5	1.12
50.8 × 38.1 × 3.18	67 500	280	287	316	8.2	13.2	28.1	1.10
50.8 × 25.4 × 3.18	66 408	276	282	295	6.3	11.4	32.2	1.05
38.1 × 38.1 × 4.76	68 744	290	297	309	6.5	13.0	29.1	1.04

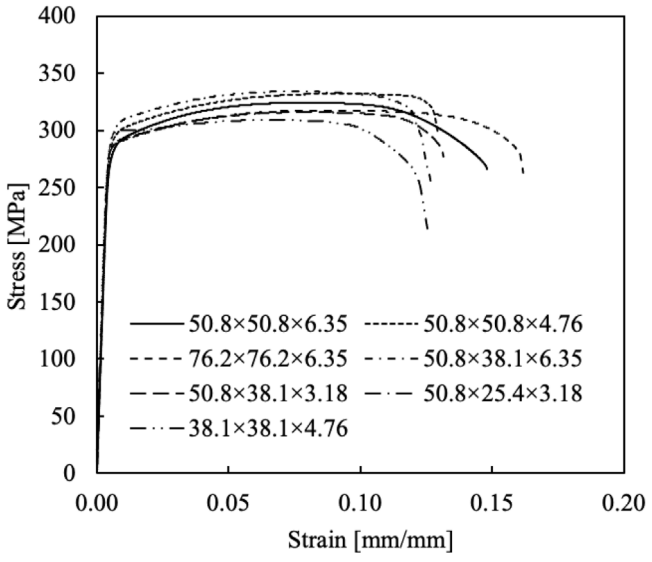

Fig. 4. Experimental stress–strain curves.

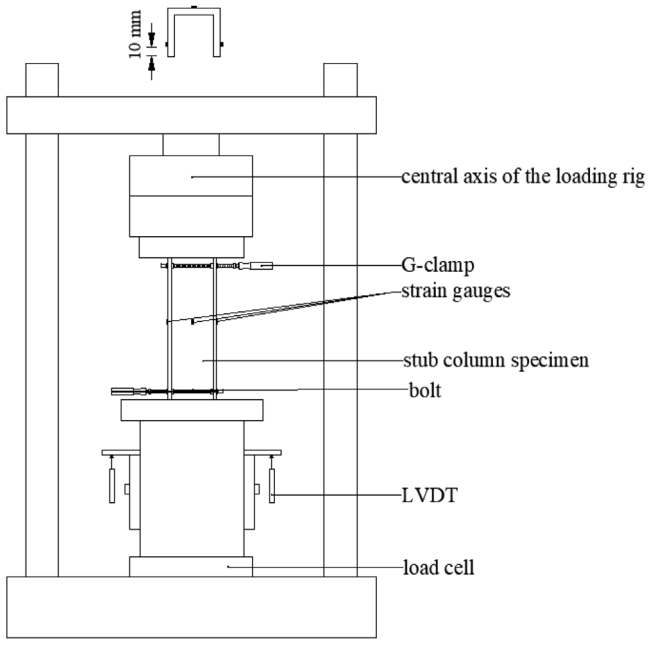

Fig. 5. Schematic illustration of the fix-ended stub column test arrangement and instrumentation.

(LVDTs) were located between the end plates to determine the end shortening of the fix-ended stub column. In addition, three linear electrical resistance strain gauges were affixed longitudinally at the mid-length of the specimen to measure the compressive strains. Particularly, the two strain gauges were affixed at both flanges at 10 mm of the tip and the third one at the middle of the web, as shown in Fig. 5. The applied loading was measured using the load cell of the machine. The applied loading, end shortening and strain values were monitored through a data acquisition equipment with sampling frequency of 10 Hz.

The load-end shortening curves (F_{cs}-δ) for all tested fix-ended stub column specimens are depicted in Fig. 7. The key tests results including the ultimate load $F_{u,cs,Exp}$ and the end shortening at ultimate load $\delta_{u,Exp}$ are summarised in Table 4. All fix-ended stub column specimens failed due to local buckling with a classic "in–out" deformation mode at the mid-length, as displayed in Fig. 8.

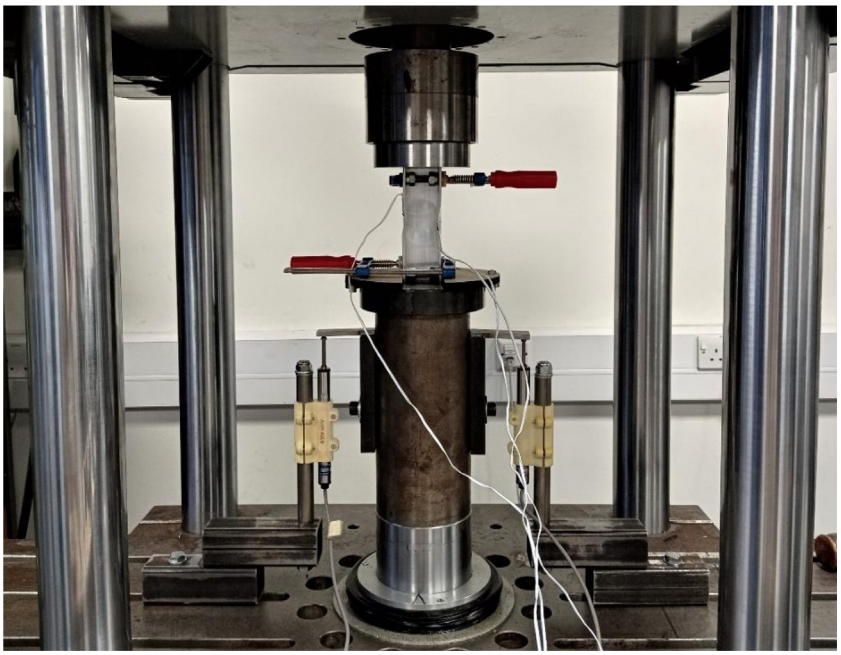

Fig. 6. Typical fix-ended stub column test setup.

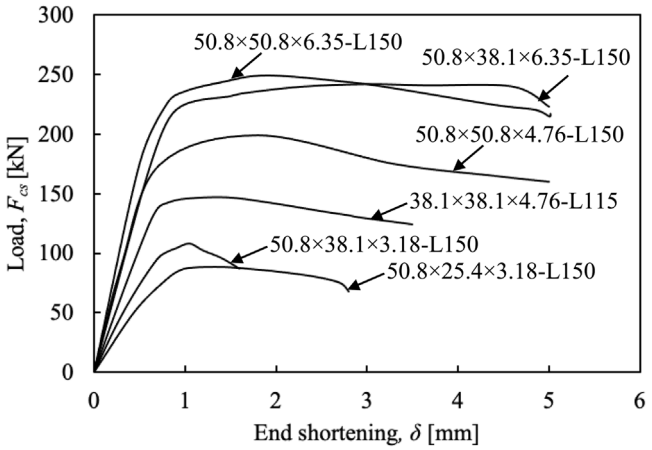

Fig. 7. Load-end shortening curves obtained from fix-ended stub column tests.

Table 4
Summary of key results obtained from fix-ended stub column tests.

Specimen	$F_{u,cs,Exp}$ (kN)	$\delta_{u,Exp}$ (mm)
50.8 × 50.8 × 6.35-L150	249.57	1.90
50.8 × 50.8 × 4.76-L150	199.10	1.80
50.8 × 38.1 × 6.35-L150	242.00	3.00
50.8 × 38.1 × 3.18-L150	108.07	1.05
50.8 × 25.4 × 3.18-L150	88.15	1.40
38.1 × 38.1 × 4.76-L115	146.65	1.45

2.4. Pin-ended column tests

Aiming to investigate the minor-axis flexural buckling, 8 C-section columns were subjected to concentric compression under pin-ended support conditions. Similar to fix-ended stub columns, the specimens were roughly cut to length and then were milled flat at both ends to ensure uniform distribution of the applied compressive loading. Fig. 9 shows a schematic illustration of the pin-ended column test arrangement and the corresponding employed instrumentation. An assembly of a pit plate with V-shaped grooves and a wedge plate with a single knife-edge wedge were used to simulate the pin-ended support conditions allowing rotation around the minor axis [38]. Moreover, the steel C-sections were loosely bolted through steel plates at both edges to clamp both specimen's ends and prevent twisting and warping.

Fig. 10 depicts the experimental setup for a typical pin-ended column test. Four LVDTs were placed; two at the mid-length to record the lateral deflection and two bilateral at the bottom edge to monitor the end rotation. Moreover, three strain gauges were attached longitudinally at the mid-length to measure the compressive strains. Particularly, the two strain gauges were affixed at both flanges at 10 mm of the tip and the third one at the middle of the web, as shown in Fig. 9. The same Mayes servo-controlled hydraulic testing machine was used to perform the compression tests applying loading at a cross-head displacement rate of 0.2 mm/min. Each specimen was placed carefully between the two pit plates and centralised in an accurate position, i.e., aimed at applied eccentricity equal to zero, using special wooden cut-outs. An initial compressive loading of approximately equal to 15% of the predicted load-carrying capacity was also applied [36] to ease the specimen's alignment into accurate position. It worth noting that the distance from the rotation centre of the knife-edge wedge to the end of the specimens was equal to 32 mm. Thus, the effective column length of each column is $L_e = L + 64$ mm, which is included in Table 2.

At initial loading stage, the readings taken from the LVDTs and strain gauges for each specimen were utilised to calculate the combined equivalent global imperfection and applied eccentricity e_m which is defined as the sum of the measured initial global geometric imperfection amplitude ω_g and the actual initial load eccentricity e_0 and is given as follows [36,39]:

$$e_m = e_0 + \omega_g = \frac{EI\left(\varepsilon_{\max} - \varepsilon_{\min}\right)}{hF_0} - \Delta \quad (1)$$

where EI is the flexural rigidity of the cross-section about the minor axis, ε_{max} is the maximum recorded compressive strain, ε_{min} is the maximum recorded tensile or minimum recorded compressive strain, h is the distance between the strain gauges attached on the web and flange, F_0 is the applied initial compressive load approximately equal to 15% of the predicted load-carrying capacity and Δ is the corresponding lateral deflection at the mid-height. Note that the e_0 value was taken as positive whether the knife-edge wedges are located closer to the flange tips (resulting initial moments lead the specimen to bow towards

Fig. 8. Failure modes obtained from fix-ended stub column tests.

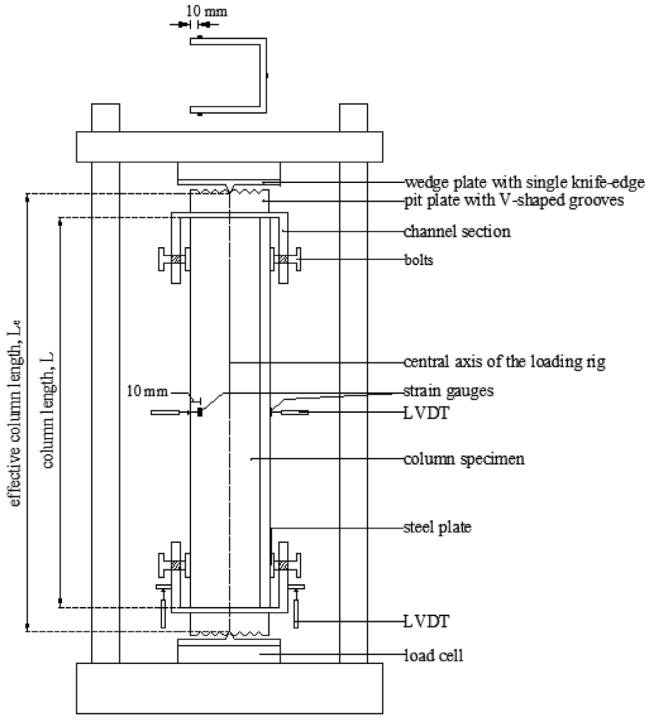

Fig. 9. Schematic illustration of the pin-ended column test arrangement and instrumentation.

Fig. 10. Typical pin-ended column test setup.

the web), whilst they are negative whether the knife-edge wedges are located closer to the web (resulting initial moments lead the specimen to bow towards the flange tips), as shown in Fig. 11.

On the basis of similar studies [14,18,36], the F_0 value was deemed adequate to ensure that the specimen's behaviour remains into the elastic range providing reliable lateral deflection and strain measurements. In case that the absolute value of the combined equivalent global imperfection and applied eccentricity $|e_m|$ exceeded the value of $L_e/1000$, the specimen's position was carefully re-adjusted to achieve $|e_m| \leq L_e/1000$ [36,40]. The final overall global geometric imperfection amplitude e_m for each examined column specimen is reported in Table 2. The applied loading, end shortening and strain values were monitored through a data acquisition equipment with sampling frequency of 10 Hz.

The recorded load-mid-height lateral deflection curves (F-Δ) for all tested columns are shown in Fig. 12. The key test results including the ultimate load $F_{u,Exp}$ and the mid-height lateral deflection at ultimate load $\Delta_{u,Exp}$ are listed in Table 5. The most common observed failure mode was global buckling accompanied by local buckling on the compressed flanges (interaction of global and local buckling). All tested specimens exhibited significant mid-height lateral deflection. Two buckling orientations were observed, namely "C" orientation and "reverse C" orientation, indicating that the specimens buckled towards the web and flange tips, respectively. Typical obtained failures modes for both buckling orientations are depicted in Fig. 13. Particularly, all specimens except 50.8 × 50.8 × 6.35-L500 specimen, had positive combined equivalent global imperfection and applied eccentricity e_m (see Table 2) and thus the additional bending moments due to second order effects induced compressive stresses at the flange tips, resulting in buckling towards the web ("C" orientation). Conversely, in 50.8 × 50.8 × 6.35-L500 specimen which had negative combined equivalent global imperfection and applied eccentricity e_m, the additional bending moments induced tensile stresses at the flange tips leading to buckling towards the flange tips ("reverse C" orientation).

3. Numerical modelling study

Aiming to investigate further the compressive behaviour of aluminium alloy columns, an extensive numerical study was carried out employing the commercial FE software ABAQUS [41]. The experimental results reported in Section 2 were utilised to validate the developed

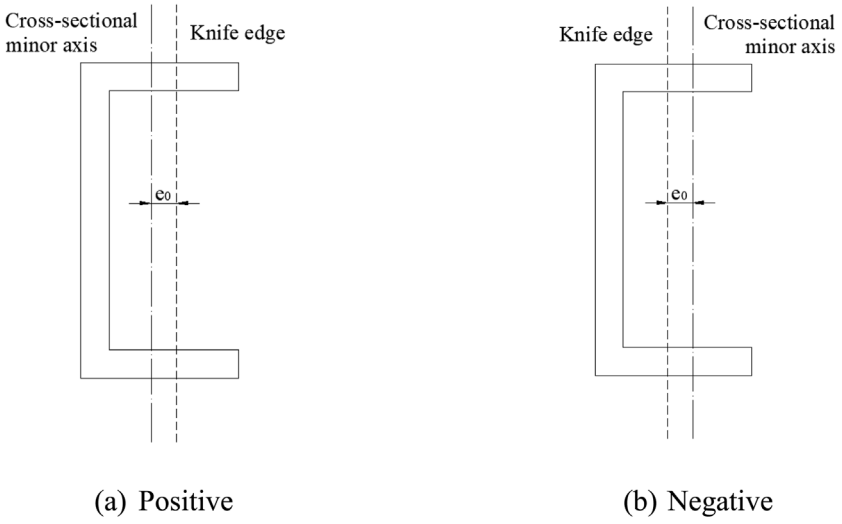

Fig. 11. Sign convention for actual initial load eccentricity e_0.

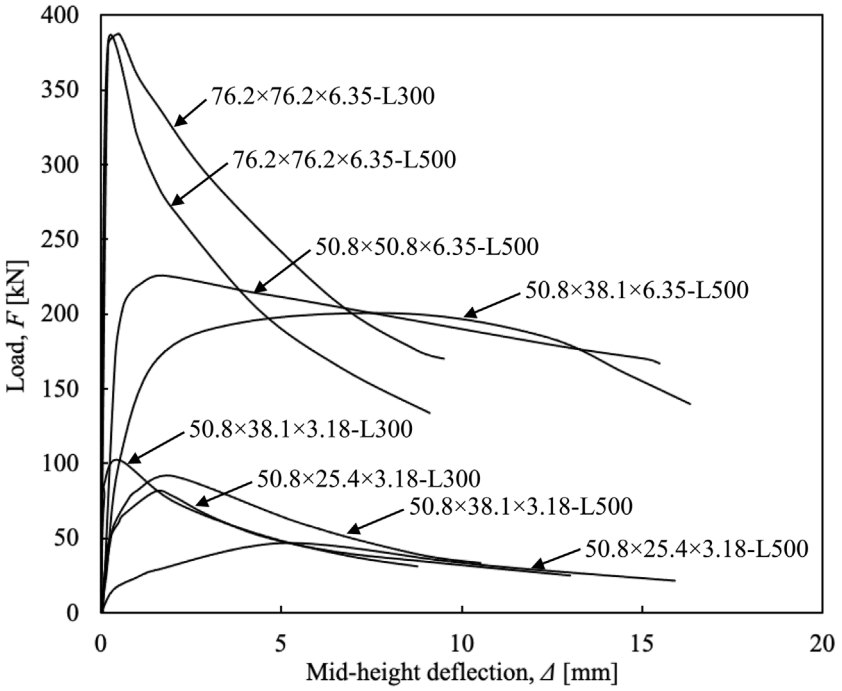

Fig. 12. Load-mid-height lateral deflection curves obtained from pin-ended column tests.

Table 5
Summary of key results obtained from flexural buckling tests.

Specimen	Orientation	$F_{u,Exp}$ (kN)	$\Delta_{u,Exp}$ (mm)
50.8 × 50.8 × 6.35-L500	"reverse C"	225.92	1.70
76.2 × 76.2 × 6.35-L500	"C"	379.63	0.20
76.2 × 76.2 × 6.35-L300	"C"	387.47	0.50
50.8 × 38.1 × 6.35-L500	"C"	200.43	8.50
50.8 × 38.1 × 3.18-L500	"C"	91.85	2.00
50.8 × 38.1 × 3.18-L300	"C"	102.50	0.50
50.8 × 25.4 × 3.18-L500	"C"	46.59	5.00
50.8 × 25.4 × 3.18-L300	"C"	81.12	1.50

FE models. Upon successful validation, the FE models were used to generate additional performance data through a series of parametric studies.

3.1. Basic modelling methodology and assumptions

Considering the thin-walled nature of C-sections and based on similar research studies [13–18,20,23], the four-node shell element with reduced integration rule (S4R) was adopted to discretise the developed FE models. A mesh convergence study was conducted to determine a mesh size that provides accurate results whilst remaining computationally efficient. A uniform mesh of 3 mm × 3 mm was found to satisfy the above requirement and thus was adopted for both the fix-ended stub and pin-ended column FE models.

The boundary conditions were defined by restraining suitable degrees of freedom according to the experimental setups. Regarding the fix-ended stub columns, all degrees of freedom were restrained at both end cross-sections, apart from the vertical translation at the loaded end. Similar boundary conditions were applied to pin-ended columns, with

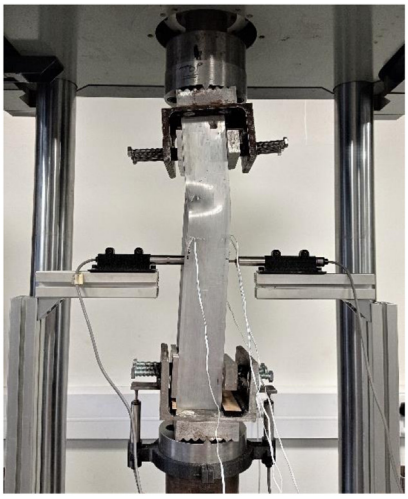

(a) 76.2×76.2×6.35-L500 - "C" orientation

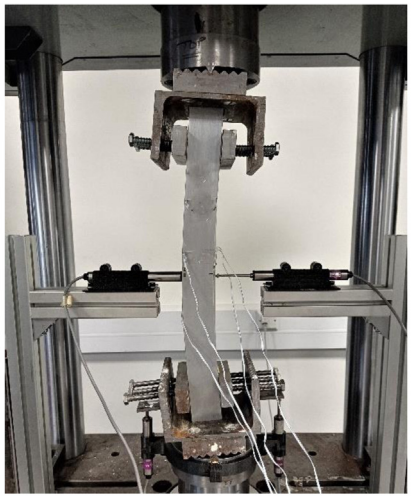

(b) 50.8×50.8×6.35-L500 - "reverse C" orientation

Fig. 13. Typical failure modes obtained from pin-ended column tests.

the only difference lying in the rotational degree of freedom about the minor axis, which was not restrained, thus allowing for modelling the pin-ended boundary conditions. The stiffening effect provided by the underpinning bolts and the G-clamps was also taken into consideration assigning distributing coupling constraints at both end cross-sections to ensure that they remain undeformed during loading. Fig. 14 displays the modelled geometry of typical fix-ended stub column and pin-ended column specimens along with the corresponding applied constraints and boundary conditions.

An elastic–plastic material model with a von Mises yield criterion and isotropic hardening rule was adopted to simulate the stress–strain behaviour of the investigated 6082-T6 heat treated aluminium alloy. The engineering stress–strain curves obtained from the tensile coupon tests were input into ABAQUS [41] in the form of true stress and logarithmic plastic strain values.

Based on the aforementioned modelling assumptions, a FE model for each tested column specimen was generated. Subsequently, a linear eigenvalue buckling analysis was carried out to extract the buckling mode shapes. These were utilised as initial geometric imperfection patterns and were incorporated into the subsequent geometrically and materially nonlinear analysis. The modified Riks solution method was employed for the nonlinear analysis allowing for capturing the full load–deformation response for each modelled column specimen. The lowest local and global buckling mode shapes were used to perturb the geometry of the pin-ended column specimens. For the fix-ended stub column specimens, only the lowest local buckling mode shape was introduced as initial local geometric imperfection pattern. An imperfection sensitivity study was also conducted for both the fix-ended stub and pin-ended columns to determine the suitable amplitude values to be adopted in the following parametric studies. For the local geometric imperfection amplitudes, three different fractions of the cross-sectional flange thickness t_f, namely t_f /15 (average measured), $t_f/50$ and $t_f/100$, were considered [42,43]. Regarding the global geometric imperfection amplitudes, three different fractions of the effective column length L_e, namely L_e /1000 (average measured), $L_e/1500$ and $L_e/2000$, were considered [28,42].

The residual stresses resulting from the heat-treatment process of the aluminium alloys were not measured in the current experimental study, because the bending residual stresses were insignificant since no pronounced curving of the tensile coupons was observed [2,44]. Moreover, it has been reported that the residual stresses have negligible influence on the ultimate strength of extruded aluminium alloy cross-sections [1]. Therefore, they were not explicitly included in the FE models developed in this study [45,46].

Table 6
Comparison between the FE and experimental ultimate loads for fix-ended stub columns.

$F_{u,cs,Exp}/F_{u,cs,FE}$			
Specimen	$t_f/15$	$t_f/50$	$t_f/100$
50.8 × 50.8 × 6.35-L150	0.97	0.99	1.0
50.8 × 50.8 × 4.76-L150	1.03	1.05	1.1
50.8 × 38.1 × 6.35-L150	1.05	1.08	1.1
50.8 × 38.1 × 3.18-L150	1.02	1.01	1.0
50.8 × 25.4 × 3.18-L150	1.05	1.10	1.1
38.1 × 38.1 × 4.76-L115	1.01	1.02	1.03
Mean	1.02	1.04	1.06
COV	0.03	0.04	0.03

3.2. Validation of the FE models

Aiming to assess the accuracy of the developed FE models and verify their suitability for the conduction of parametric studies, the numerical results were compared with those obtained from tests. Tables 6 and 7 present the ratios of the experimental $F_{u,cs,Exp}$ ($F_{u,Exp}$) over the FE $F_{u,cs,FE}$ ($F_{u,FE}$) ultimate strengths for the considered imperfection amplitudes for the fix-ended stub and pin-ended columns, respectively. It can be seen that the values of the initial imperfection amplitudes slightly influence the $F_{u,cs,Exp}/F_{u,cs,FE}$ and $F_{u,Exp}/F_{u,FE}$ ratios. The most accurate and consistent prediction of the experimental response for the fix-ended stub columns is obtained for the average measured local imperfection amplitude $t_f/15$ which resulted in mean value and corresponding coefficient of variation (COV) of the $F_{u,cs,Exp}/F_{u,cs,FE}$ ratio of 1.02 and 0.03, respectively. For the flexural buckling column tests, the average measured local $t_f/15$ and global $L_e/1000$ imperfection amplitudes provided the best agreement between the experimental and FE response with mean value and corresponding coefficient of variation (COV) of the $F_{u,Exp}/F_{u,FE}$ ratio of 1.00 and 0.03, respectively.

Typical load–deformation curves obtained from tests and FE analyses are depicted in Fig. 15. It can be seen that the compressive behaviour was accurately predicted throughout the loading history, including the initial stiffness, ultimate load, displacement corresponding to ultimate load and inelastic response exhibited during the tests. Moreover, a good agreement was achieved between the experimental and FE failure modes, as shown in Fig. 16. It can be concluded that the developed FE models can accurately replicate the cross-sectional and flexural buckling response of aluminium alloy C-sections.

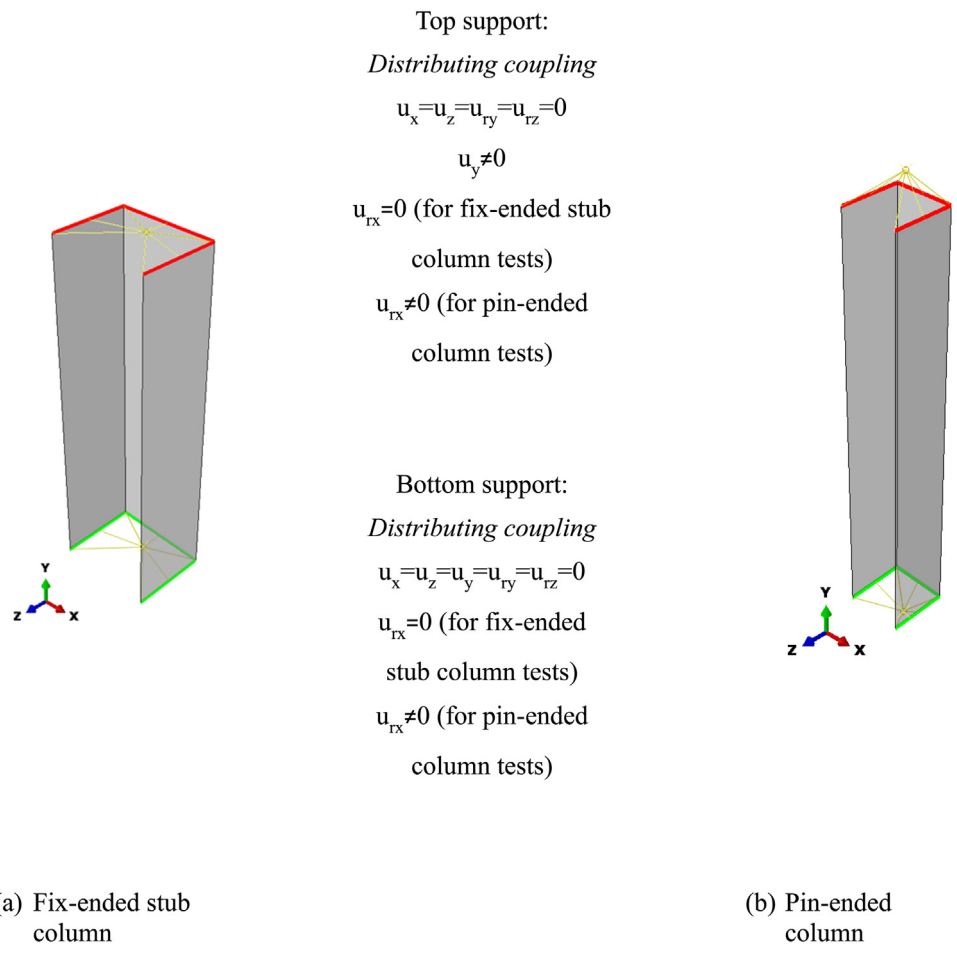

Fig. 14. Modelled geometry of typical specimens and the corresponding applied constraints and boundary conditions.

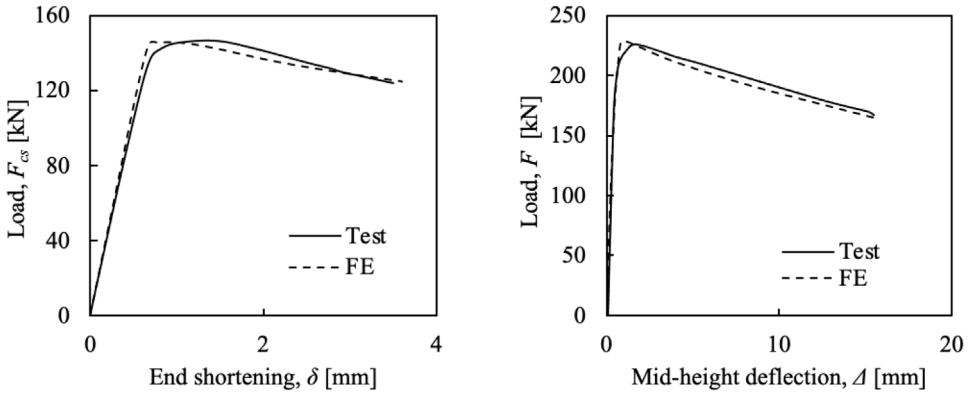

Fig. 15. Comparison between typical FE and experimental load–deformation curves for (a) stub fix-ended columns and (b) pin-ended columns.

3.3. Parametric studies

Upon validation of the developed FE models, parametric studies were performed for both fix-ended stub and pin-ended columns. The generated FE models adhere to the modelling assumptions described in Section 3.1. For the fix-ended stub columns, five different aspect ratios, *D/B,* were considered keeping the outer web depth *D* fixed to 150 mm, whilst the outer flange width *B* was ranging from 150 to 50 mm. The plate thickness varied from 2.5 to 22.0 mm to encompass a wide range of cross-sectional slenderness ratios β_f/ε and cross-sectional slendernesses λ_l (see Section 4.2.1). Note that the FE models used in the parametric studies were validated against experimental results with cross-sectional slenderness ratios β_f/ε ranging from 5.46 to 11.94. Following the practice applied in similar FE studies [13,15,20], the cross-section slenderness has been extended to a wider range (β_f/ε:1.36–52.50) in the numerical parametric study. The length of the fix-ended stub columns was set equal to 450 mm which is three times the maximum cross-sectional dimension to ensure pure local buckling behaviour without any coupled instability phenomena [26]. For the pin-ended columns, three different cross-sections were examined,

(a) 50.8×50.8×6.35-L150

(b) 76.2×76.2×6.35-L300

Fig. 16. Comparison between typical experimental (left) and FE (right) failure modes for (a) stub fix-ended columns and (b) pin-ended columns.

namely $100 \times 100, 100 \times 67$ and 100×50, with corresponding aspect ratios D/B of 1.0, 1.5 and 2.0, respectively. Moreover, three plate thicknesses of 10, 13 and 16 mm were examined. The members' length L was ranging from 600 to 1800 mm providing a broad range of member slendernesses $\overline{\lambda}$ from 0.36–2.04 and column slenderness parameters $\overline{\lambda}_c$ (see Section 4.2.2) from 0.39–2.04. Tables 8 and 9 list the examined parameters considered for the columns.

The material properties adopted in the parametric studies were based on the averaged stress–strain curves obtained from the tensile coupon tests of this study. The initial local geometric imperfections were accounted for through the lowest buckling mode shape with an amplitude of $t_f/15$ for the fix-ended stub and pin-ended columns, respectively, whereas the global imperfection amplitude for the pin-ended columns was taken as $L_e/1000$. A total of 47 and 45 numerical analyses were carried out for the fix-ended stub and pin-ended columns, respectively. The obtained results are discussed in Section 4.

4. Assessment of Eurocode 9 and direct strength method

In this section, the accuracy of the Eurocode 9 (EC9) [24] design provisions, including the flexural buckling curve, is assessed on the basis of the experimentally and numerically obtained ultimate strengths. The applicability of the DSM [25] on the design of aluminium alloy C-sections subjected to concentric compression is also evaluated. It is

Table 7
Comparison between the FE and experimental ultimate loads for pin-ended columns for local imperfection amplitude $t_f/15$.

$F_{u,Exp}/F_{u,FE}$			
Specimen	$L_e/1000$	$L_e/1500$	$L_e/2000$
50.8 × 50.8 × 6.35-L500	0.99	1.01	1.02
76.2 × 76.2 × 6.35-L500	1.03	1.04	1.04
76.2 × 76.2 × 6.35-L300	1.01	1.04	1.04
50.8 × 38.1 × 6.35-L500	0.96	0.97	0.99
50.8 × 38.1 × 3.18-L500	1.02	1.05	1.07
50.8 × 38.1 × 3.18-L300	1.03	1.05	1.06
50.8 × 25.4 × 3.18-L500	0.99	0.99	1.00
50.8 × 25.4 × 3.18-L300	0.96	1.00	1.04
Mean	1.00	1.02	1.03
COV	0.03	0.03	0.03

Table 8
List of key parameters considered in parametric studies for fix-ended stub columns.

	Total FE analyses: 47
5 aspect ratios D/B (D × B):	• 1.0 (150 × 150) • 1.25 (150 × 120) • 1.5 (150 × 100) • 2.0 (150 × 75) • 3.0 (150 × 50)
Thicknesses ($t_f = t_w$) (mm)	• 2.5–22.0
Resulting slenderness ratio β_f/ε	• β_f/ε: 1.36–52.50
Resulting cross-sectional slendernesses λ_l	• λ_l: 0.19–2.49

Table 9
List of key parameters considered in parametric studies for pin-ended columns.

	Total FE analyses: 45
3 aspect ratios D/B (D × B):	• 1.0 (100 × 100) • 1.5 (100 × 67) • 2.0 (100 × 50)
Thicknesses ($t_f = t_w$) (mm)	• 10, 13, 16
Column lengths L (mm)	• 600–1800
Resulting member slendernesses $\bar{\lambda}$	• $\bar{\lambda}$: 0.36–2.04
Resulting column slenderness parameter $\bar{\lambda}_c$	• $\bar{\lambda}_c$: 0.39–2.04

noted that throughout the comparisons all partial safety factors were set equal to unity.

4.1. Eurocode 9

4.1.1. Cross-sectional compressive resistance

EC9 [24] estimates the compressive resistance of a cross-section considering the material yield strength and the susceptibility of each constituent plate element to local buckling. Particularly, EC9 [24] classifies the cross-sections in four different classes based on slenderness limits and thus identifies to what extent the cross-sectional resistance is limited by the local buckling resistance. Classes 1, 2 and 3 or stocky cross-sections are able to achieve their proof strength, whilst Class 4 or slender cross-sections fail prior to the attainment of their yield strength, owing to significant local buckling phenomena which govern their ultimate behaviour. According to Section 6.2.4 specified in EC9 [24], the resistance $F_{pred,cs,EC9}$ of C-sections subjected to uniform compression is estimated as follows:

$$F_{pred,cs,EC9} = F_{pl,Rk} = \begin{cases} A\sigma_{0.2} & \text{for Classes 1, 2, 3} \\ A_{eff}\sigma_{0.2} & \text{for Class 4} \end{cases} \quad (2)$$

where A_{eff} is the effective cross-sectional area calculated by assuming a reduced thickness for the slender plate elements through a reduction factor ρ_c:

$$\rho_c = \frac{C_1}{(\beta_f/\varepsilon)} - \frac{C_2}{(\beta_f/\varepsilon)^2} \quad (3)$$

where the constants C_1 and C_2 were taken equal to 10 and 24, respectively.

Table 10 lists the predicted-to-ultimate ratios $F_{pred,cs,EC9}/F_{u,cs}$ together with the corresponding slenderness parameter β_f/ε of the flange. The values of the ultimate resistance $F_{u,cs}$ were provided by the results of tests and the parametric study. It can be seen that EC9 [24] provides safe design strength predictions but quite conservative with a mean value of the $F_{pred,cs,EC9}/F_{u,cs}$ ratio equal to 0.85 (much lower than unity). The same can also be concluded from Fig. 17 which presents the $F_{pred,cs,EC9}/F_{u,cs}$ ratios plotted against the β_f/ε values. This graph shows clearly that the level of conservatism of the EC9 increases for slender cross-sections, i.e., cross-sections with higher β_f/ε values. This could be attributed to the fact that the additional data were generated based on FE models which were validated against experimental results with low β_f/ε values, whilst the imperfection amplitude was considered the same for both stocky and slender cross-sections. It might be possible that the influence of the geometric imperfection amplitude to be more evident for cross-sections with higher β_f/ε values and thus resulting in more conservative design strength predictions. Additionally, the relatively low coefficient of variation (COV) of 0.11 and the apparent scattering of the data points plotted in Fig. 17 confirm the relatively low level of design consistency provided by the EC9 [24].

4.1.2. Flexural buckling resistance

According to Section 6.3.1 specified in EC9 [24], the design flexural buckling resistance $F_{pred,EC9}$ of C-section members subjected to uniform compression is estimated as follows:

$$F_{pred,EC9} = \chi F_{pl,Rk} \quad (4)$$

where the reduction coefficient χ is given by Eq. (5).

$$\chi = \frac{1}{\phi + \left[\phi^2 - \bar{\lambda}^2\right]^{0.5}} \leq 1.0 \quad (5)$$

The parameter ϕ can be estimated by Eq. (6) and the member slenderness $\bar{\lambda}$ is defined in Section 2.1.

$$\phi = 0.5\left[1 + \alpha\left(\bar{\lambda} - \bar{\lambda}_0\right) + \bar{\lambda}^2\right] \quad (6)$$

where α and $\bar{\lambda}_0$ is the imperfection factor and the limit of the horizontal plateau, respectively, corresponding to the relevant buckling curve (for 6082-T6 α is 0.2 and $\bar{\lambda}_0$ is 0.1).

The applicability of the EC9 [24] design buckling curve is evaluated by comparing the obtained ultimate strengths F_u derived from pin-ended column tests and FE models with the respective codified predicted resistances $F_{pred,EC9}$. To do so, the F_u values were normalised by the corresponding plastic resistance $F_{pl,Rk}$ values and were plotted against the member slenderness $\bar{\lambda}$ as shown in Fig. 18. It can be seen that both the experimental and FE data points are above the design curve, suggesting that the design strength predictions are safe but conservative. The predicted-to-ultimate $F_{pred,EC9}/F_u$ ratios are also presented in Table 11 together with the corresponding member slenderness $\bar{\lambda}$ values. The resulted mean value of 0.87 of the $F_{pred,EC9}/F_u$ ratio denotes that EC9 [24] underestimates the actual flexural buckling resistance of 6082-T6 aluminium alloy columns. Moreover, the corresponding COV value of 0.08 together with the scattered data points displayed in Fig. 18 suggest relatively low level of design consistency of EC9 [24] strength predictions.

Aiming to improve the accuracy level of the current design rules provided by EC9 [24], the obtained experimental and FE results were utilised to propose a revised flexural buckling curve for Class A aluminium alloys. In particular, a revised imperfection factor α of 0.16 and a revised limit of the horizontal plateau $\bar{\lambda}_0$ of 0.2 are proposed providing the best agreement between the EC9 [24] strength predictions and the experimental and FE results. The proposed flexural buckling curve is plotted in Fig. 18, whilst the proposed predicted-to-ultimate ratios

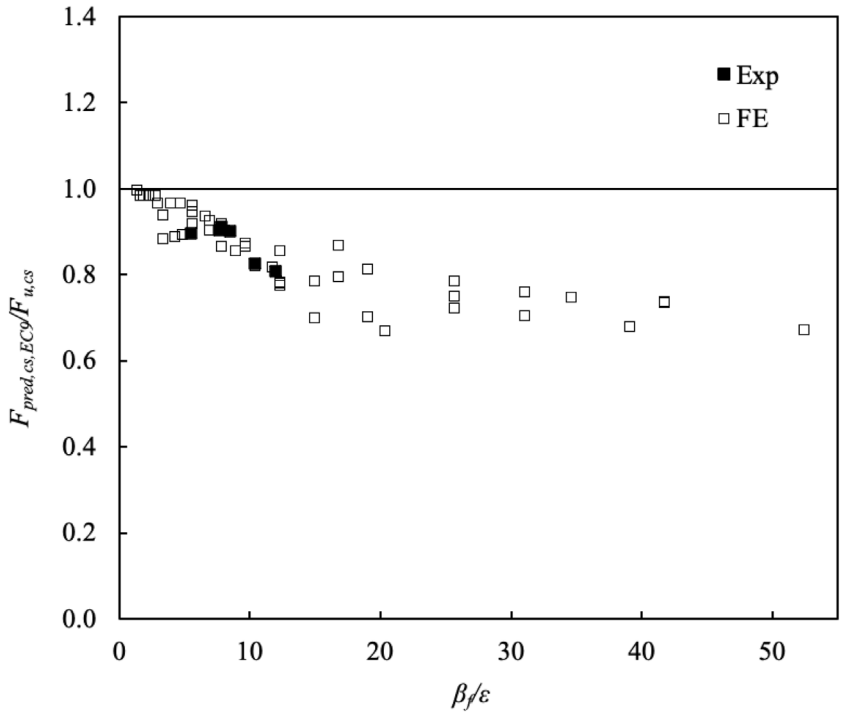

Fig. 17. Comparison of experimental and FE results with EC9 [24] design strengths for fix-ended stub columns.

Table 10
Predicted strength ratios for both experimental and numerical results for fix-ended stub columns.

Specimen	No	Eurocode 9		Direct strength method	
		β_f/ε	$F_{pred,cs,EC9}/F_{u,cs}$	λ_l	$F_{pred,cs,DSM}/F_{u,cs}$
50.8 × 50.8 × 6.35-L150	1	7.49	0.90	0.35	1.00
50.8 × 50.8 × 4.76-L150	1	10.42	0.83	0.48	0.99
50.8 × 38.1 × 6.35-L150	1	5.46	0.89	0.32	0.89
50.8 × 38.1 × 3.18-L150	1	11.94	0.81	0.68	1.00
50.8 × 25.4 × 3.18-L150	1	7.62	0.90	0.58	0.95
38.1 × 38.1 × 4.76-L115	1	7.84	0.91	0.37	0.98
FE	47	1.36–52.50	0.85	0.19–2.49	0.96
		Mean (all)	0.85		0.96
		COV (all)	0.11		0.04

Table 11
Predicted strength ratios for both experimental and numerical results for pin-ended columns.

Specimen	No	Eurocode 9			Direct strength method	
		$\bar{\lambda}$	$F_{pred,EC9}/F_u$	$F_{pred,EC9,prop}/F_u$	$\bar{\lambda}_c$	$F_{pred,DSM}/F_u$
50.8 × 50.8 × 6.35-L500	1	0.63	0.90	0.94	0.65	0.94
76.2 × 76.2 × 6.35-L500	1	0.36	0.76	0.78	0.40	0.96
76.2 × 76.2 × 6.35-L300	1	0.22	0.77	0.79	0.24	0.98
50.8 × 38.1 × 6.35-L500	1	0.90	0.78	0.83	0.90	0.79
50.8 × 38.1 × 3.18-L500	1	0.79	0.75	0.79	0.86	0.89
50.8 × 38.1 × 3.18-L300	1	0.48	0.78	0.81	0.51	0.95
50.8 × 25.4 × 3.18-L500	1	1.32	0.78	0.82	1.34	0.91
50.8 × 25.4 × 3.18-L300	1	0.79	0.77	0.82	0.80	0.81
FE	45	0.36–2.04	0.88	0.93	0.39–2.04	0.93
		Mean (all)	0.87	0.91		0.93
		COV (all)	0.08	0.07		0.06

$F_{pred,EC9,prop}/F_u$ are included in Table 11. As can be seen, the achieved mean value of the $F_{pred,EC9,prop}/F_u$ ratio is 0.91 which is higher than that of the $F_{pred,EC9}/F_u$ ratio signifying that the proposed curve offers slightly more accurate strength predictions. The same can be drawn from Fig. 18 where the data points are closer to the proposed buckling curve.

4.2. Direct strength method

4.2.1. Cross-sectional compressive resistance

The DSM is codified in Section E3.2.1 of [22] as an alternative and simplified design method for prediction of the cross-sectional compressive resistance of cold-formed carbon steel cross-sections. This

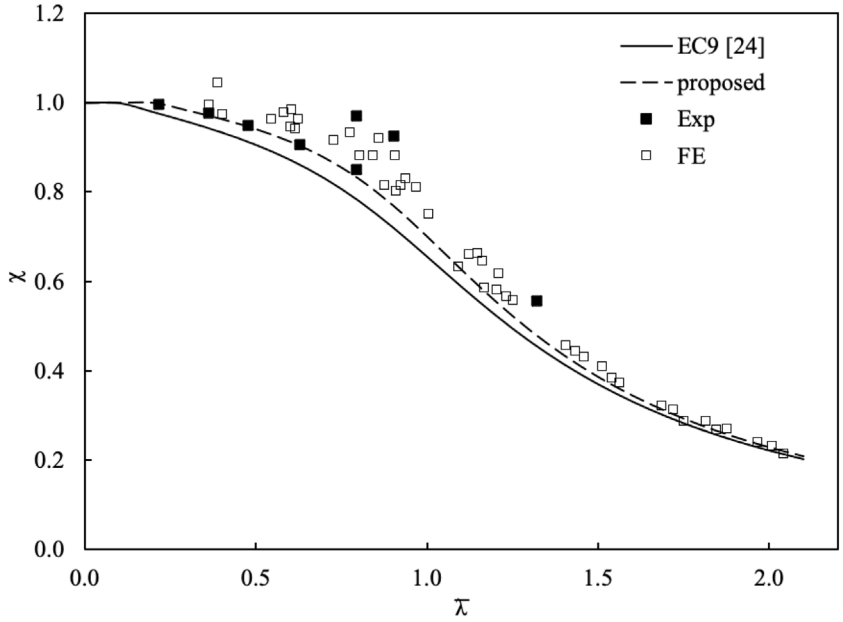

Fig. 18. Comparison of experimental and FE results with EC9 [24] design strength predictions for pin-ended columns.

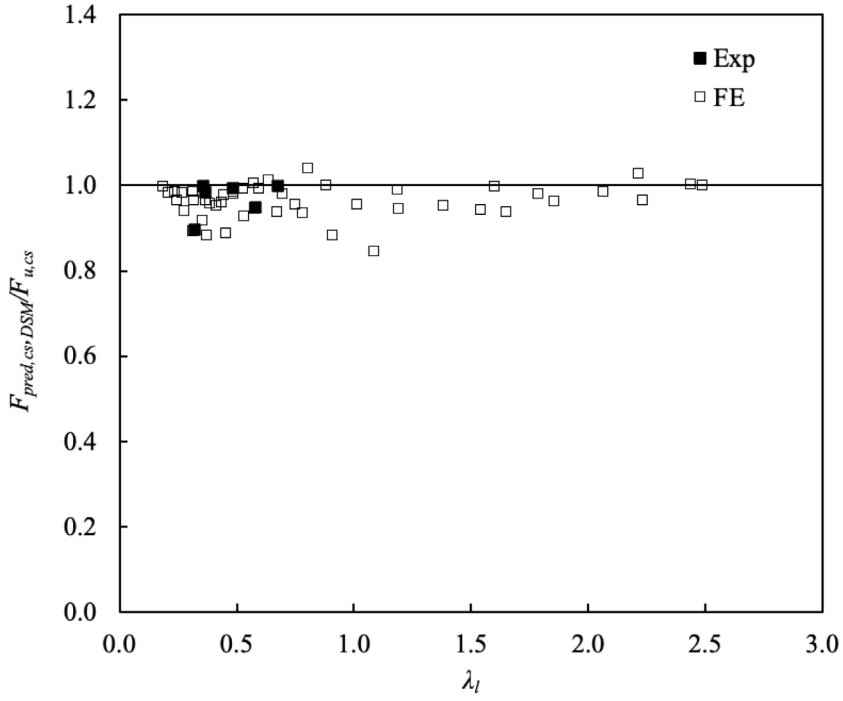

Fig. 19. Comparison of experimental and FE results with DSM [22] design strengths for fix-ended stub columns.

method utilises the cross-sectional slenderness λ_l and adopts a 'strength curve' allowing to directly determine the cross-sectional compressive resistance $F_{DSM,cs,pred}$ of a slender cross-section ($\lambda_l > 0.776$). In case of a stocky cross-section ($\lambda_l \leq 0.776$), the cross-sectional compressive resistance $F_{DSM,cs,pred}$ equals to the yield strength $A\sigma_{0.2}$ of the cross-section. The design formulae for both stocky and slender cross-sections are given by Eq. (7):

$$F_{DSM,cs,pred} = \begin{cases} A\sigma_{0.2} & \text{for } \lambda_l \leq 0.776 \\ \left[1 - 0.15\left(\frac{F_{crl}}{A\sigma_{0.2}}\right)^{0.4}\right]\left(\frac{F_{crl}}{A\sigma_{0.2}}\right)^{0.4} A\sigma_{0.2} & \text{for } \lambda_l > 0.776 \end{cases} \quad (7)$$

where $\lambda_l = \sqrt{F_{ne}/F_{crl}}$, $F_{ne} = A\sigma_{0.2}$ is the flexural buckling strength defined in Section 4.2.2 and $F_{crl} = A\sigma_{cr}$ is the critical elastic local column buckling load where σ_{cr} is the elastic critical buckling stress of the cross-section. The stress σ_{cr} accounts for the element interaction and can be obtained using either proposed analytical formulae [47] or numerical tools, such as CUFSM [48].

The predicted-to-ultimate $F_{pred,cs,DSM}/F_{u,cs}$ ratios along with the corresponding cross-sectional slenderness λ_l values are provided in Table 10. The resulted mean value of the $F_{pred,cs,DSM}/F_{u,cs}$ ratio is 0.96 and the corresponding COV is 0.04 denoting that the DSM offers significantly more precise and consistent strength predictions compared to EC9 [24] ($F_{pred,cs,EC9}/F_{u,cs} = 0.85$ and corresponding COV = 0.11). Moreover, in Fig. 19 the $F_{pred,cs,DSM}/F_{u,cs}$ ratios are plotted against

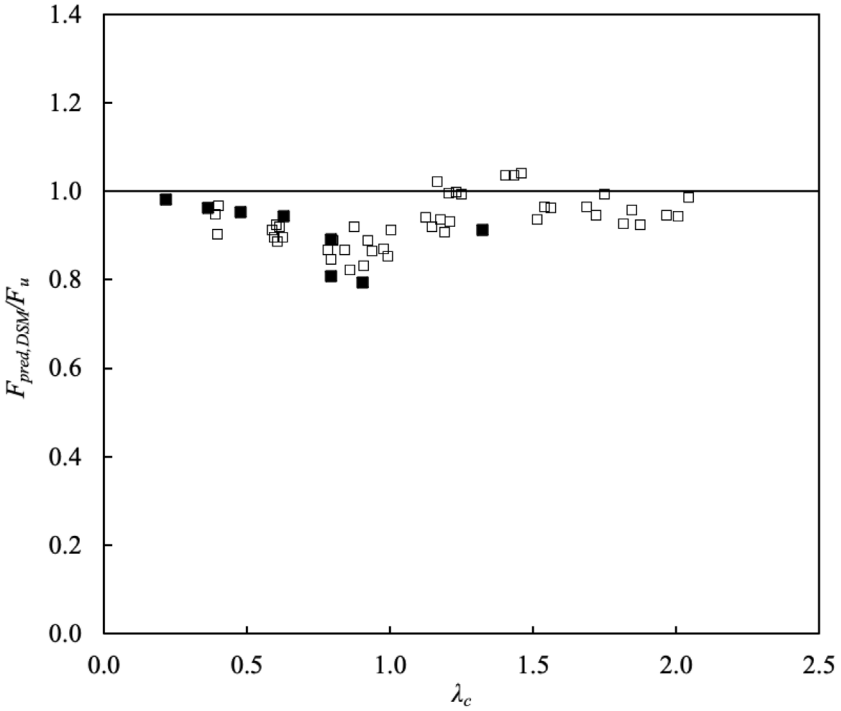

Fig. 20. Comparison of experimental and FE results with DSM [22] design strengths for pin-ended columns.

the cross-sectional slenderness λ_l values. Again, it can be concluded that the DSM provides higher design accuracy and consistency than EC9 [24] as the data points are closer to unity and less scattered.

4.2.2. Flexural buckling resistance

According to Section E.2 specified in DSM [22], the flexural buckling resistance $F_{pred,DSM}$ of C-section members subjected to uniform compression could be calculated as follows:

$$F_{pred,DSM} = F_{ne} = \begin{cases} \left(0.658^{\lambda_c^2}\right) A\sigma_{0.2} & \text{for } \lambda_c \le 1.5 \\ \left(\dfrac{0.877}{\lambda_c^2}\right) A\sigma_{0.2} & \text{for } \lambda_c > 1.5 \end{cases} \quad (8)$$

where $\lambda_c = \sqrt{A\sigma_{0.2}/F_{cre}}$ is the column slenderness parameter and F_{cre} is the least of the applicable elastic flexural buckling stresses calculated in accordance with Sections E2.1 and E2.2 of [22].

Fig. 20 displays the $F_{pred,DSM}/F_u$ ratios plotted against column slenderness parameter λ_c values suggesting that the DSM [22] provides accurate and relatively low scattered design strength predictions. Furthermore, Table 11 provides the predicted-to-ultimate $F_{pred,DSM}/F_u$ ratios along with the corresponding column slenderness parameter λ_c values. As can be seen the DSM [22] design rules exhibit the most accurate design strength predictions with mean value of the $F_{pred,DSM}/F_u$ ratio of 0.93. Higher design consistency is also provided since the corresponding COV is 0.06 which is the lowest values amongst those resulted from EC9 [24] and the revised EC9 design rules proposed herein.

5. Conclusions

The present paper reports 6 fix-ended stub columns tests and 8 pin-ended column tests on 6082-T6 heat-treated aluminium alloy C-sections. The obtained experimental results were utilised to develop FE models considering material and geometrical nonlinearities. A subsequent numerical study was conducted generating 92 additional performance data over a wide range of cross-sectional aspect ratios, and cross-sectional and member slendernesses. The experimentally and numerically derived ultimate strengths were used to assess the accuracy of the Eurocode 9 design provisions. A new flexural buckling curve is proposed based on both the experimental and numerical results improving the design accuracy by 5%. The applicability of the DSM for cold-formed carbon steel cross-sections was also evaluated finding that it is suitable for the design of aluminium alloy C-sections subjected to concentric compression. Relative comparisons between EC9 and DSM design strengths denoted that the DSM provides more accurate predictions, i.e., predicted-to-ultimate strength ratios of 0.96 and 0.93 for fix-ended stub and pin-ended columns, respectively.

CRediT authorship contribution statement

Evangelia Georgantzia: Writing – original draft, Visualization, Validation, Software, Methodology, Investigation, Formal analysis, Data curation, Conceptualization. **Michaela Gkantou:** Writing – review & editing, Visualization, Supervision, Methodology, Funding acquisition, Conceptualization. **George S. Kamaris:** Writing – review & editing, Supervision, Funding acquisition.

Declaration of competing interest

The authors declare that they have no known competing financial interests or personal relationships that could have appeared to influence the work reported in this paper.

Data availability

Data will be made available on request.

Acknowledgements

The authors are grateful to the technicians of the Departments of Civil Engineering and Mechanical Engineering at Liverpool John Moores University for their valuable assistance. The financial support of the Faculty of Engineering and Technology of Liverpool John Moores University, United Kingdom is gratefully acknowledged.

References

[1] F.M. Mazzolani, Aluminum Alloy Structures, second ed., E & FN Spon, London, 1995.

[2] K.J.R. Rasmussen, G.J. Hancock, Design of thin-walled plain channel section columns against flexural buckling, Thin-Walled Struct. 20 (1–4) (1994) 219–240.

[3] B. Young, Rasmussen, Tests of fixed-ended plain channel columns, J. Struct. Eng. 124 (2) (1998) 131–139.

[4] B. Young, K.J.R. Rasmussen, Shift of effective centroid of channel columns, J. Struct. Eng. ASCE. 125(5) (199) 524–531.

[5] B. Young, J. Yan, Finite element analysis and design of fixed-ended plain channel columns, Finite Elem. Anal. Des. 38 (6) (2002) 549–566.

[6] B. Young, P.B. Dinis, D. Camotim, CFS lipped channel columns affected by $L-D-G$ interaction. Part I: Experimental investigation, Comput. Struct. 207 (2018) 219–232.

[7] P.B. Dinis, D. Camotim, B. Young, E.M. Batista, CFS lipped channel columns affected by $L-D-G$ interaction. Part II: Numerical simulations and design considerations, Comput. Struct. 207 (2018) 200–218.

[8] J. Ye, I. Hajirasouliha, J. Becque, Experimental investigation of local-flexural interactive buckling of cold-formed steel channel columns, Thin-Walled Struct. 125 (2018) 245–258.

[9] D. Yang, G.J. Hancock, Compression tests of high strength steel channel columns with interaction between local and distortional buckling, J. Struct. Eng. ASCE 130 (12) (2004) 1954–1963.

[10] NAS, North American Specification for the Design of Cold-Formed Steel Structural Members, American Iron and Steel Institute, Washington DC, 2001.

[11] B.W. Schafer, T. Peköz, Direct strength prediction of cold-formed steel members using numerical elastic buckling solutions, in: Int Spec Conf Cold-Formed Steel Struct Recent Res Dev Cold-Formed Steel Des Constr, 1998, pp. 69–76.

[12] J. Becque, K.J.R. Rasmussen, A numerical investigation of local-overall interaction buckling of stainless steel lipped channel columns, J. Constr. Steel Res. 65 (8–9) (2009) 1685–1693.

[13] F. Wang, O. Zhao, B. Young, Testing and numerical modelling of S960 ultra-high strength steel angle and channel section stub columns, Eng. Struct. 204 (2020) 109902.

[14] F. Wang, Y. Liang, O. Zhao, Experimental and numerical studies of pin-ended press-braked S960 ultra-high strength steel channel section columns, Eng. Struct. 215 (2020) 110629.

[15] L. Zhang, F. Wang, Y. Liang, O. Zhao, Press-braked S690 high strength steel equal-leg angle and plain channel section stub columns: Testing, numerical simulation and design, Eng. Struct. 201 (2019) 109764.

[16] European Committee for Standarization (EC3), Eurocode 3: Design of Steel Structures, Part 1-3: General Rules-Supplementary Rules for Cold-Formed Members and Sheeting, BS EN 1993-1-3:2005, CEN:2005, BSI, 2005.

[17] L. Zhang, K.H. Tan, O. Zhao, Local stability of press-braked stainless steel angle and channel sections: Testing, numerical modelling and design analysis, Eng. Struct. 203 (2020) 109869.

[18] L. Zhang, K.H. Tan, O. Zhao, Press-braked stainless steel channel section columns failing by flexural buckling: Testing, numerical simulation and design, Thin-Walled Struct. 157 (2020) 107066.

[19] E. Georgantzia, M. Gkantou, G.S. Kamaris, Aluminium alloys as structural material: A review of research, Eng. Struct. 227 (2021) 111372.

[20] J.H. Zhu, Z.Q. Li, M.N. Su, B. Young, Behaviour of aluminium alloy plain and lipped channel columns, Thin-Walled Struct. 135 (2019) 306–316.

[21] M.N. Su, B. Young, L. Gardner, The continuous strength method for the design of aluminium alloy structural elements, Eng. Struct. 122 (2016) 338–348.

[22] NAS, North American Specification for the Design of Cold-Formed Steel Structural Members, American Iron and Steel Institute, Washington DC, 2012.

[23] J.H. Zhu, Z.-Q. Li, M.-N. Su, B. Young, Numerical study and design of aluminium alloy channel section columns with welds, Thin-Walled Struct. 139 (2019) 139–150.

[24] European Committee for Standarization (EC9), Eurocode 9 : Design of Aluminium Structures, Part 1-1: General Structural Rules - General Structural Rules and Rules for Buildings, BS EN 1999-1-1:2007, CEN:2007, 2007.

[25] AISI North American Specification for the Design of Cold-Formed Steel Structural Members, Washington DC, USA, 2016.

[26] R. Ziemian, Guide to Stability Design Criteria for Metal Structures, sixth ed., John Wiley & Sons, Inc, 2010.

[27] Y. Zhao, X. Zhai, J. Wang, Buckling behaviors and ultimate strengths of 6082-T6 aluminum alloy columns under eccentric compression – part I : Experiments and finite element modeling, Thin-Walled Struct. 143 (2019).

[28] Y. Zhao, X. Zhai, L. Sun, Test and design method for the buckling behaviors of 6082-T6 aluminum alloy columns with box-type and L-type sections under eccentric compression, Thin-Walled Struct. 100 (2016) 62–80.

[29] E. Georgantzia, M. Gkantou, G.S. Kamaris, K. Kansara, K. Hashim, Aluminium alloy cross-sections under uniaxial bending and compression: A numerical study, in: IOP Conf. Ser.: Mater. Sci. Eng, Vol. 1058, 2021, 012011.

[30] E. Georgantzia, M. Gkantou, G.S. Kamaris, Numerical modelling and design of aluminium alloy angles under uniform compression, CivilEng. 2 (3) (2021) 632–651.

[31] E. Georgantzia, M. Gkantou, G.S. Kamaris, K. Kansara, Design of aluminium alloy channel sections under minor axis bending, Thin-Walled Struct. 174 (2022) 109098.

[32] Y. Sun, A. He, Y. Liang, O.O. Zhao, Flexural buckling behaviour of high-chromium stainless steel welded I-section columns, Thin-Walled Struct. 154 (2020) 106812.

[33] European Committee for Standardization (CEN), Metallic Materials – Tensile Testing – Part 1, Method of Test At Room Temperature, Brussels, 2009.

[34] W. Ramberg, W.R. Osgood, Description of Stress–Strain Curves By Three Parameters, Vol. Technical, National Advisory Committe for Aeronautics, Washington, D.C, 1943.

[35] H.N. Hill, J.W. Clark, R.J. Brungraber, Design of welded aluminum structures, J. Struct. Div. ASCE 86 (6) (1960) 101–124.

[36] C. Buchanan, E. Real, L. Gardner, Testing, simulation and design of cold-formed stainless steel CHS columns, Thin-Walled Struct. 30 (2018) 297–312.

[37] M. Theofanous, T.M. Chan, L. Gardner, Structural response of stainless steel oval hollow section compression members, Eng. Struct. 31 (4) (2009) 922–934.

[38] E. Georgantzia, S. Bin Ali, M. Gkantou, G.S. Kamaris, K. Kansara, W. Atherton, Flexural buckling performance of concrete-filled aluminium alloy tubular columns, Eng. Struct. 242 (2021) 112546.

[39] M. Chen, B. Young, Experimental and numerical investigation on cold-formed steel semi-oval hollow section compression members, J. Constr. Steel Res. 151 (2018) 174–184.

[40] K.J.R. Rasmussen, G.J. Hancock, Tests of high strength steel columns, J. Constr. Steel Res. 34 (1995) 27–52.

[41] Karlsson, Hibbit, Sorensen, ABAQUS:Theory Manual, Providence, RI, USA, Dassault Systemes Corporation, 2018.

[42] R. Feng, W. Zhu, H. Wan, A. Chen, Y. Chen, Tests of perforated aluminium alloy SHSs and RHSs under axial compression, Thin-Walled Struct. 130 (2018) 194–212.

[43] J.H. Zhu, B. Young, Numerical investigation and design of aluminum alloy circular hollow section columns, Thin-Walled Struct. 46 (2008) 1437–1449.

[44] M. Jandera, L. Gardner, J. Machacek, Residual stresses in cold-rolled stainless steel hollow sections, 64 (2008) 1255–1263.

[45] R. Feng, J. Liu, Numerical investigation and design of perforated aluminium alloy SHS and RHS columns, Eng. Struct. 199 (2019).

[46] F. Wang, B. Young, L. Gardner, Compressive testing and numerical modelling of concrete-filled double skin CHS with austenitic stainless steel outer tubes, Thin Walled Struct. 141 (2019) 345–359.

[47] M. Seif, B.W. Schafer, Local buckling of structural steel shapes, J. Constr. Steel Res. 66 (10) (2010) 1232–1247.

[48] Z. Li, B.W. Schafer, Buckling analysis of cold-formed steel members with general boundary conditions using CUFSM: conventional and constrained finite strip methods, in: 20th International Specialty Conference on Cold-Formed Steel Structures. St. Louis, Missouri, U.S.A, 2010.